# NOTES AND CORRESPONDENCE

## NAM Model Forecasts of Warm-Season Quasi-Stationary Frontal Environments in the Central United States

SHIH-YU WANG

*Utah Climate Center, Utah State University, Logan, Utah*

ADAM J. CLARK

*National Severe Storms Laboratory, Norman, Oklahoma*

(Manuscript received 18 December 2009, in final form 17 March 2010)

ABSTRACT

Using a composite procedure, North American Mesoscale Model (NAM) forecast and observed environments associated with zonally oriented, quasi-stationary surface fronts for 64 cases during July–August 2006–08 were examined for a large region encompassing the central United States. NAM adequately simulated the general synoptic features associated with the frontal environments (e.g., patterns in the low-level wind fields) as well as the positions of the fronts. However, kinematic fields important to frontogenesis such as horizontal deformation and convergence were overpredicted. Surface-based convective available potential energy (CAPE) and precipitable water were also overpredicted, which was likely related to the overprediction of the kinematic fields through convergence of water vapor flux. In addition, a spurious coherence between forecast deformation and precipitation was found using spatial correlation coefficients. Composite precipitation forecasts featured a broad area of rainfall stretched parallel to the composite front, whereas the composite observed precipitation covered a smaller area and had a WNW–ESE orientation relative to the front, consistent with mesoscale convective systems (MCSs) propagating at a slight right angle relative to the thermal gradient. Thus, deficiencies in the NAM precipitation forecasts may at least partially result from the inability to depict MCSs properly. It was observed that errors in the precipitation forecasts appeared to lag those of the kinematic fields, and so it seems likely that deficiencies in the precipitation forecasts are related to the overprediction of the kinematic fields such as deformation. However, no attempts were made to establish whether the overpredicted kinematic fields actually contributed to the errors in the precipitation forecasts or whether the overpredicted kinematic fields were simply an artifact of the precipitation errors. Regardless of the relationship between such errors, recognition of typical warm-season environments associated with these errors should be useful to operational forecasters.

### 1. Introduction

Seasonal precipitation exhibits a maximum center over the upper Midwest during midsummer (July–August). This precipitation center occurs in close association with the northward extension of the low-level jet (LLJ) and the retreat of the upper-level jet stream (e.g., Higgins et al. 1997; Wang and Chen 2009). Such a circulation evolution forms a preferred time frame for the "warm-season pattern," consisting of a slow-moving ridge over the western United States and a synoptic trough over the eastern United States, with prevailing northwesterly flow in the midtroposphere and an east–west-oriented, quasi-stationary front near the surface (Johns 1993). Low-level warm advection along the quasi-stationary front and northwesterly shear provide favorable conditions for progressive mesoscale convective systems (MCSs) (Johns and Hirt 1987; Schmidt and Cotton 1989; Smull and Augustine 1993; Coniglio and Stensrud 2001; Coniglio et al. 2004). In addition, moisture pooling by low-level convergence along the northern terminus of the LLJ (Segal et al. 1989) creates large convective available potential energy (CAPE) with low convective inhibition

*Corresponding author address:* Shih-Yu (Simon) Wang, Utah Climate Center, Utah State University, 4825 Old Main Hill, Logan, UT 84322-4825.
E-mail: simon.wang@usu.edu

DOI: 10.1175/2010WAF2222394.1

for the MCS development (Weisman 1990; Knievel and Johnson 2002). MCSs developing under these specific conditions contribute to about 60% of the midsummer rainfall over the upper Midwest (Wang et al. 2010), which accounts for most of the 75% contribution from all MCSs estimated by Fritsch et al. (1986).

It is known that numerical weather prediction (NWP) models do not simulate warm-season convective rainfall well (e.g., Fritsch and Carbone 2004). This deficiency is attributed to rapid error growth associated with convective processes (e.g., Walser et al. 2004; Kong et al. 2006; Hohenegger and Schar 2007), inability to properly depict finescale and/or subtle forcing mechanisms [e.g., outflow boundaries, drylines, or midtropospheric perturbations (Wang et al. 2009, 2010)], and difficulties in handling planetary boundary layer evolution (e.g., Bukovsky et al. 2006; Coniglio et al. 2009). Further difficulties in forecasting warm-season precipitation in current operational NWP models such as the National Centers for Environmental Prediction (NCEP) North American Mesoscale Model (NAM; Janjić 2003) arise from the use of cumulus parameterization (CP), which is needed to depict the effects of subgrid-scale convective processes (e.g., Molinari and Dudek 1992). Specifically, previous works (e.g., Davis et al. 2003; Clark et al. 2007, 2009) find that models that utilize CP struggle in replicating well-organized propagating convective systems, which struggle is likely related to inadequate resolution of downdrafts that lead to the cold pool dynamics associated with propagation (Davis et al. 2003), as well as other deficiencies inherently linked to the CPs [e.g., crude trigger functions (Liu et al. 2006), lack of mesoscale organization (Molinari and Dudek 1992), and independent activation of the schemes in individual grid columns (Bukovsky et al. 2006)].

Upon routine inspection of operational forecasts during typical warm-season regimes favorable for progressive MCSs, we have noticed that NAM has a tendency to generate spurious elongated ''rainbands'' along quasi-stationary surface boundaries in the Upper Midwest, a previously undocumented feature (to the best of our knowledge) that is examined herein. These rainbands do not reflect propagating MCSs that are observed in such cases; rather they are nonpropagating features closely tied to simulated low-level frontogenesis. Two representative cases in which these spurious rainbands were observed are provided in Figs. 1 and 2. In the first case, which occurred on 20 August 2007, an observed MCS traveled along a quasi-stationary front that stretched across Iowa and Illinois (Figs. 1a and 1b). The 24-h NAM forecast depicted the key synoptic features of the associated warm-season pattern, including the quasi-stationary boundary (Fig. 1d). However, the forecasts did not capture the propagating MCS, but instead generated an elongated frontal rainband stretching across the Upper Midwest and the Ohio Valley. At 900 hPa and slightly north of the surface front, the NAM generates a pronounced frontal zone (Fig. 1e) in terms of horizontal deformation (DEF)[1] and horizontal gradient of potential temperature ($|\nabla\theta|$)—fields commonly used in depicting fronts (e.g., Martin 2006). The 900-hPa DEF and $|\nabla\theta|$ appear to be spatially coherent with the forecast rainband, whereas in the analysis (Fig. 1c) DEF and $|\nabla\theta|$ are not as strong and are much less coherent with the observed rainfall (Fig. 1b). A different case on 24 August 2006 (Fig. 2) reveals similar behavior in the NAM: a spurious rainband and a strong relationship between the rainband and the 900-hPa DEF in the forecast. However, in this second case the coherence between $|\nabla\theta|$ and rainfall is not as robust as in the first. It is not clear whether the enhanced low-level frontal zones are simply an artifact of the spurious rainbands, or if the reverse occurs and the spurious rainband are related to the overpredicted low-level DEF and $|\nabla\theta|$ fields.

The goal of this study is to thoroughly document forecast and observed environmental conditions associated with warm-season quasi-stationary boundaries in the central United States. A composite approach is utilized to reveal the general features of these simulated and observed quasi-stationary boundaries. Particular emphasis will be placed on the pervasiveness of the aforementioned spurious rainbands and the characteristics of the associated frontal zones. Because the operational NAM affects a large and diverse group of users and because model configurations similar to the NAM are used in operational ensemble systems like NCEP's Short-Range Ensemble Forecast (SREF) system (Du et al. 2004), diagnosing specific model behaviors/deficiencies can be very beneficial. The study is arranged as follows: data and methods are introduced in section 2, analysis results are shown and discussed in section 3, and a summary is given in section 4.

## 2. Data and methods

### *a. Data*

Operational NAM forecasts are obtained from the National Oceanic and Atmospheric Administration National Operational Model Archive and Distribution System (NOMADS; information online at http://nomads.ncdc.noaa.gov). Currently, the Weather Research and Forecasting (WRF) nonhydrostatic mesoscale model is run as the NAM, which has 12-km grid spacing, 45

[1] Deformation $= \{[(\partial u/\partial x) - (\partial v/\partial y)]^2 + [(\partial v/\partial x) + (\partial u/\partial y)]^2\}^{1/2}$.

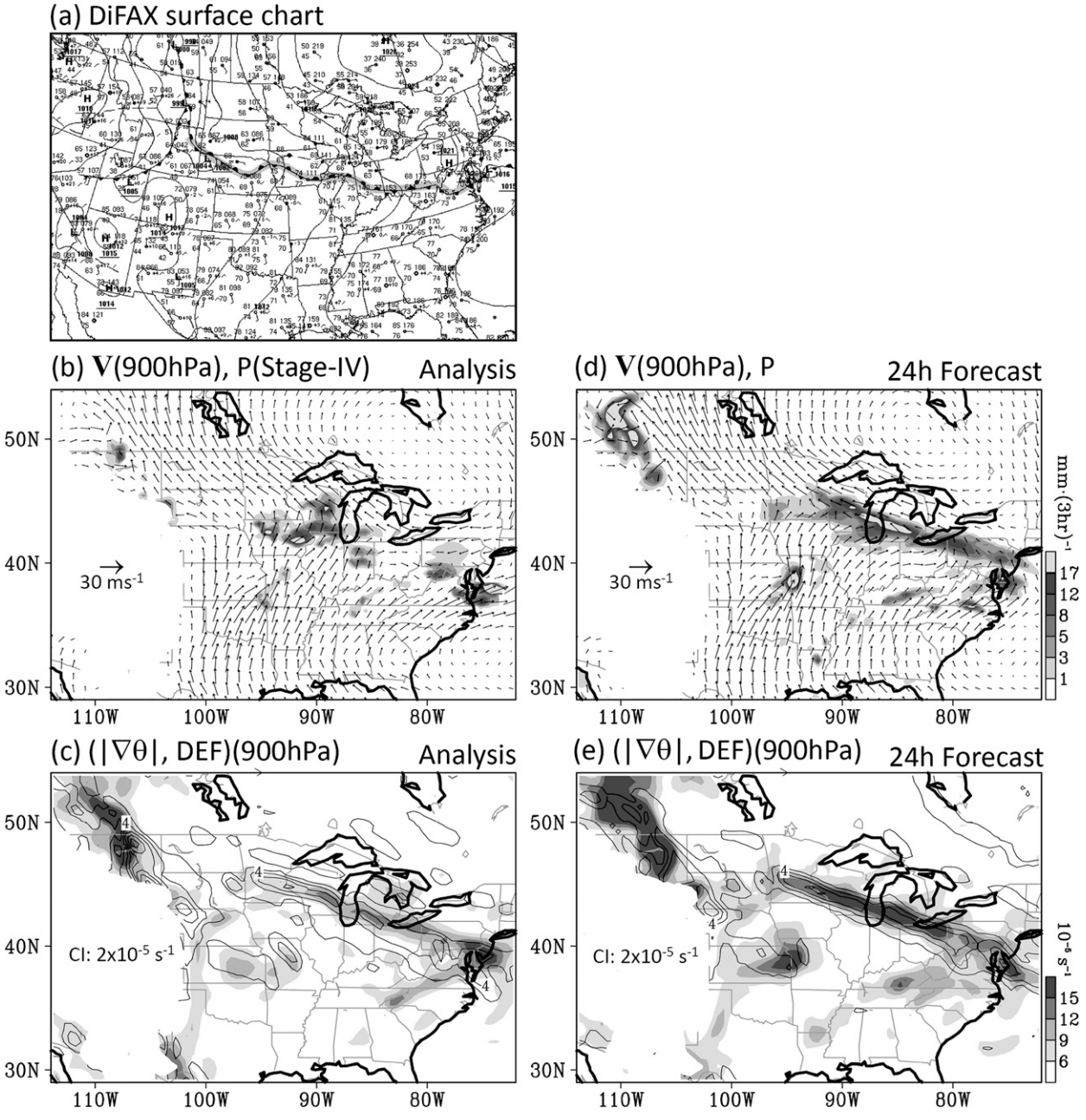


FIG. 1. (a) DiFAX surface chart at 0600 UTC 20 Aug 2007, and NAM analysis of (b) 900-hPa wind vectors superimposed with 3-h accumulated stage-IV precipitation (shadings) and (c) 900-hPa potential temperature gradient (contours) and horizontal deformation (shadings). (d),(e) As in (b) and (c), but for the 24-h NAM forecast with 3-h accumulated precipitation (initialized 0600 UTC 19 Aug 2007).

vertical levels, and is run four times daily with 3-hourly output available. Physics schemes used in NAM include the Betts–Miller–Janjić (BMJ; Betts 1986; Betts and Miller 1986; Janjić 1994) cumulus parameterization, the Ferrier et al. (2002) microphysics scheme, and a Mellor–Yamada–Janjić (MYJ; Mellor and Yamada 1982; Janjić 2002) boundary layer parameterization. Stage-IV multisensor rainfall estimates (Lin and Mitchell 2005) are used for precipitation observations and are remapped to the 12-km grid of the NAM using a neighbor-budget interpolation that conserves the total amount of liquid in the domain (e.g., Accadia et al. 2003). The stage-IV data are obtained from NCEP (online at http://www.emc.ncep.noaa.gov). The National Weather Service U.S. ''Surface Analysis

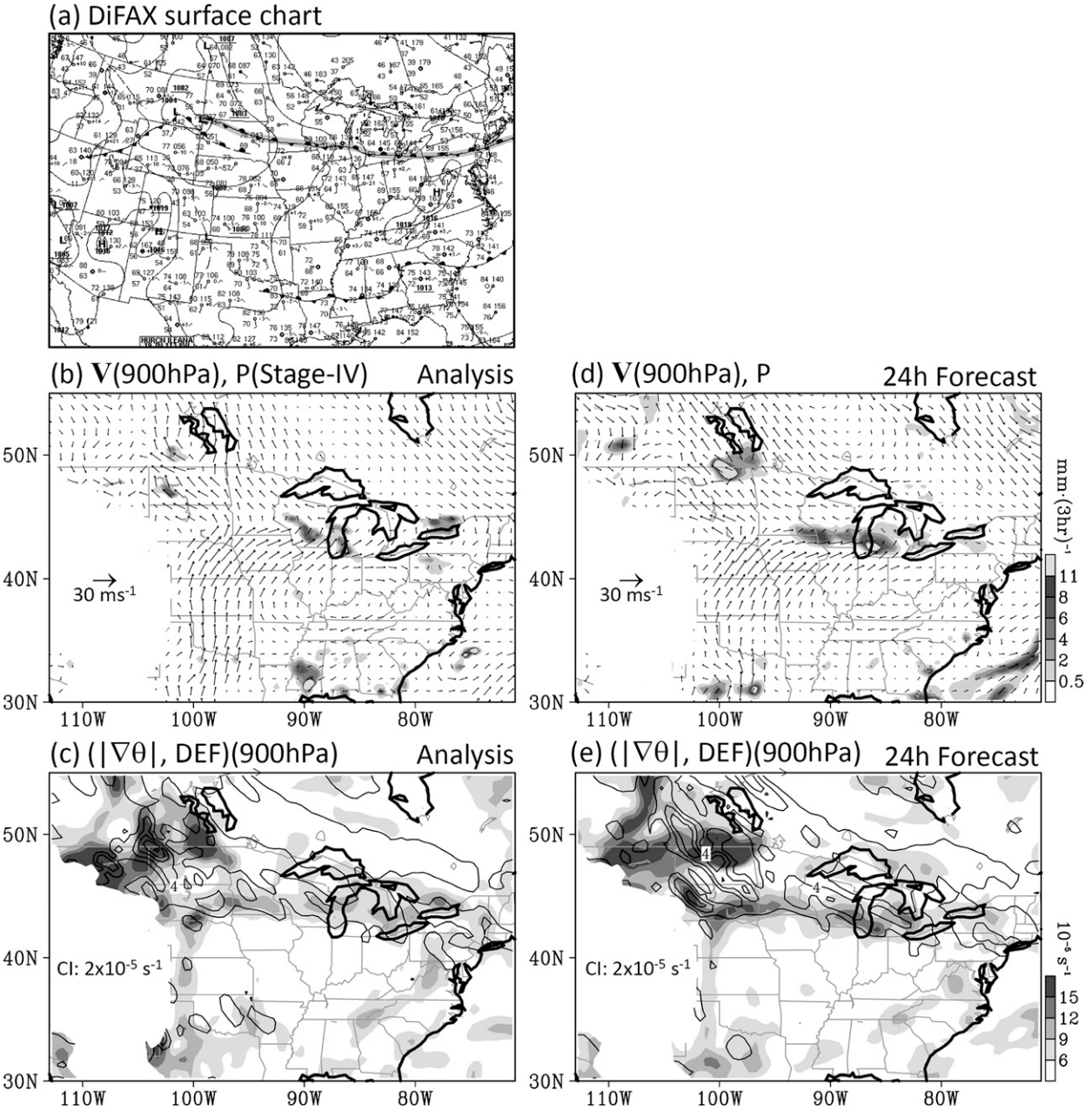


FIG. 2. As in Fig. 1, but for the 0600 UTC 24 Aug 2006 case.

Charts" (formerly known as digital facsimiles or DiFAX), used here for frontal identification, are obtained from the Department of Atmospheric Science, Colorado State University (online at http://archive.atmos.colostate.edu/). The analysis period covers July–August 2006–08.

### b. *Frontal composite procedure*

To identify cases for inclusion in frontal composites, quasi-stationary fronts as depicted by the Surface Analysis Charts are examined for a region east of the Rocky Mountains and west of the East Coast between 35° and 50°N at 0000, 0600, 1200, and 1800 UTC during the analysis period. For inclusion in the composites, a quasi-stationary front must have east–west orientation *within* an angle that is ±30° relative to lines of latitude. For example, the stationary fronts in cases 1 and 2 (Figs. 1a and 2a, respectively) are both WNW–ESE oriented with an angle of about −10° relative to lines of latitude. In addition, the fronts must exist for at least 24 h and must

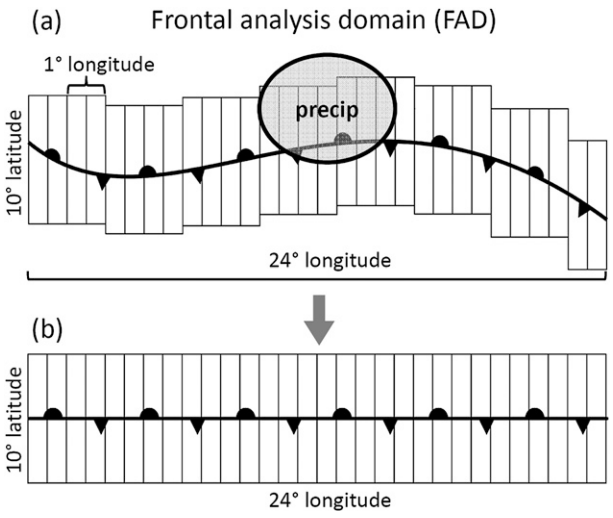


FIG. 3. Schematic illustrations of the FAD and its "cells" (a) before and (b) after alignment, and its position relative to precipitation (see text).

stretch for more than 10° in the zonal direction. Last, to restrict our analysis to cases that fit within the warm-season pattern, the 500-hPa wind direction over the center of the fronts must be westerly to northwesterly (270°–330°), based on the NAM analysis. Cold fronts associated with migrating/developing synoptic waves are not included. Because frontal composites for both forecasts and observations are constructed relative to the position of observed fronts, the effectiveness of the composite procedure is dependent on the position of forecast quasi-stationary fronts closely corresponding to the observed fronts. Based on a subjective examination of all cases, as well as the close correspondence of spatial patterns between composite forecast and observed fields such as low-level winds (Figs. 4a and 4f, discussed below), the NAM does in fact produce reasonable forecasts for the positions of such fronts.

A frontal analysis domain (FAD) is defined for each identified front, as illustrated by the schematic diagram in Fig. 3a. The FAD covers a 10° latitude × 24° longitude area with the latitudinal center defined by the frontal position and the longitudinal center decided by the maximum precipitation along/near the front. The precipitation $P$ maximum is determined by an inverse Laplace transform, $\nabla^{-2}P$, using the inverse Fourier transform. The use of $\nabla^{-2}P$ allows for an objective method in determining the $P$ center and is especially useful when the rainfall pattern is spotty and often migrating. Because $P$ accumulated over a 24-h period (0000–2300 UTC) is used, each FAD during a 24-h period has a fixed longitudinal center. If no precipitation occurs within the FAD, or if the maximum daily precipitation is under 0.5 cm, then the zonal midpoint of this front is used as the FAD center. Table 1 lists the dates, the center coordinates, and the schematic general orientations of the identified quasi-stationary fronts.

Next, the FAD is partitioned into 48 "cells," each comprising a domain of 10° latitude × 0.5° longitude with the quasi-stationary front through its meridional midpoint. These uniformly partitioned FAD cells are manually centered along the front's contour, as shown in Fig. 3a. These FAD cells are applied to both the NAM analysis and forecast based on the observed front. The purpose of the partitioning is to realign individual fronts onto a rectangular domain, as shown in Fig. 3b, so that frontal composites can be constructed. During the steps from Fig. 3a to Fig. 3b, both the precipitation and NAM data are bilinearly interpolated onto a 0.25° × 0.25° grid, so that each FAD cell has 2 grid points zonally and 40 meridionally. If a front stretches longer than 24° longitude, only the portion of the front within the 24° of longitude is used. If a front spans less than 24° in longitude, then we record as far as the front reaches in the zonal direction. As a result, composite fields within outer FAD cells have been obtained using fewer cases than for inner FAD cells and are therefore less representative.

### c. *Frontogenesis*

While surface fronts are commonly depicted by horizontal deformation and horizontal gradient of potential temperature ($\nabla\theta$), the intensification or decay of a front is represented by the frontogenetic tendency $D|\nabla\theta|/Dt$ or frontogenesis (e.g., Martin 2006), expressed as

$$\frac{D|\nabla\theta|}{Dt} = T_1 + T_2 + T_3 + T_4 \cdots. \tag{1}$$

In Eq. (1),

$$T_1 = \mathbf{n} \cdot \nabla Q, \tag{2}$$

where $\mathbf{n}$ is a unit vector in the direction of $\nabla\theta$ and $Q$ is the diabatic heating rate obtained from the residual method of the thermodynamic equation;

$$T_2 = \frac{\partial\theta}{\partial p}\mathbf{n} \cdot \nabla\omega, \tag{3}$$

where $\omega$ is the vertical velocity in pressure coordinates;

$$T_3 = -\frac{1}{2}|\nabla\theta|\nabla \cdot \mathbf{V}; \tag{4}$$

TABLE 1. Date, center coordinate, and general orientation of the quasi-stationary fronts analyzed. Fronts that tilt within ±15°, greater than 15° and less than −15° relative to lines of latitude are schematically represented by a dash (—), a back slash (\), and a forward slash (/), respectively.

| Date | Center position | Orientation | Date | Center position | Orientation |
|---|---|---|---|---|---|
| 3 Jul 2006 | 42.1°N, 92.9°W | — | 6 Aug 2007 | 41.1°N, 91.1°W | — |
| 4 Jul 2006 | 39.5°N, 92.3°W | — | 7 Aug 2007 | 44.3°N, 89.9°W | / |
| 10 Jul 2006 | 37.4°N, 94.8°W | / | 8 Aug 2007 | 41.6°N, 92.1°W | — |
| 11 Jul 2006 | 42.2°N, 93.3°W | — | 9 Aug 2007 | 42.5°N, 90.4°W | / |
| 12 Jul 2006 | 42.9°N, 84.3°W | — | 13 Aug 2007 | 41.8°N, 93.5°W | — |
| 18 Jul 2006 | 41.3°N, 88.5°W | — | 15 Aug 2007 | 41.2°N, 92.8°W | — |
| 20 Jul 2006 | 43.2°N, 92.4°W | / | 16 Aug 2007 | 42.0°N, 93.8°W | — |
| 21 Jul 2006 | 39.8°N, 92.2°W | — | 19 Aug 2007 | 44.2°N, 90.1°W | — |
| 22 Jul 2006 | 37.1°N, 88.1°W | / | 20 Aug 2007 | 42.5°N, 90.8°W | — |
| 25 Jul 2006 | 44.4°N, 94.2°W | — | 22 Aug 2007 | 43.2°N, 91.5°W | — |
| 29 Jul 2006 | 46.5°N, 94.1 °W | — | 23 Aug 2007 | 43.8°N, 91.5°W | / |
| 2 Aug 2006 | 45.1°N, 91.5°W | / | 6 Jul 2008 | 46.1°N, 92.7°W | / |
| 3 Aug 2006 | 42.1°N, 90.4°W | / | 7 Jul 2008 | 41.8°N, 91.5°W | / |
| 7 Aug 2006 | 39.6°N, 92.4°W | — | 9 Jul 2008 | 38.6°N, 92.8°W | — |
| 8 Aug 2006 | 40.0°N, 93.1°W | — | 10 Jul 2008 | 47.1°N, 93.6°W | — |
| 10 Aug 2006 | 41.7°N, 92.9°W | — | 16 Jul 2008 | 45.3°N, 93.4°W | — |
| 18 Aug 2006 | 41.3°N, 91.4°W | — | 17 Jul 2008 | 45.2°N, 93.0°W | — |
| 19 Aug 2006 | 41.1°N, 90.6°W | / | 18 Jul 2008 | 42.1°N, 91.9°W | / |
| 23 Aug 2006 | 47.5°N, 92.5°W | \ | 19 Jul 2008 | 41.8°N, 92.8°W | — |
| 24 Aug 2006 | 45.1°N, 93.9°W | — | 20 Jul 2008 | 41.8°N, 92.6°W | \ |
| 25 Aug 2006 | 44.0°N, 90.4°W | / | 21 Jul 2008 | 42.2°N, 90.1°W | — |
| 9 Jul 2007 | 42.2°N, 93.7°W | / | 22 Jul 2008 | 39.7°N, 91.8°W | — |
| 14 Jul 2007 | 44.9°N, 88.7°W | — | 25 Jul 2008 | 40.3°N, 87.5°W | \ |
| 16 Jul 2007 | 44.8°N, 95.3°W | \ | 26 Jul 2008 | 38.9°N, 86.7°W | / |
| 17 Jul 2007 | 39.1°N, 90.4°W | — | 27 Jul 2008 | 43.5°N, 96.1°W | — |
| 18 Jul 2007 | 40.4°N, 88.2°W | — | 28 Jul 2008 | 41.0°N, 91.9°W | — |
| 19 Jul 2007 | 41.1°N, 92.9°W | — | 29 Jul 2008 | 42.5°N, 94.7°W | — |
| 20 Jul 2007 | 36.6°N, 91.2°W | — | 4 Aug 2008 | 44.3°N, 90.8°W | / |
| 27 Jul 2007 | 41.2°N, 92.3°W | / | 5 Aug 2008 | 41.9°N, 89.5°W | — |
| 28 Jul 2007 | 37.9°N, 89.0°W | — | 6 Aug 2008 | 38.5°N, 95.2°W | — |
| 4 Aug 2007 | 45.3°N, 95.8°W | \ | 14 Aug 2008 | 43.9°N, 93.1°W | / |
| 5 Aug 2007 | 45.2°N, 95.3°W | \ | 23 Aug 2008 | 42.1°N, 93.5°W | / |

and

$$T_4 = \frac{1}{2}|\nabla\theta||\mathrm{DEF}|\cos(2\lambda), \quad (5)$$

where DEF is the horizontal deformation and $\lambda$ is the angle between the dilatation axis and the potential isotherms. This derivation follows Hanstrum et al. (1990). Here, $T_1$ represents the contribution to frontogenesis of horizontal gradients in diabatic heating, $T_2$ refers to the rate of frontogenesis due to the tilting of vertical $\theta$ gradients through horizontal gradients of vertical velocity, $T_3$ is frontogenesis through horizontal convergence of the potential isotherms, and $T_4$ indicates frontogenesis owing to horizontal deformation of the $\theta$ distribution. It will be shown that the latter two terms—in particular $T_4$—are the dominant factors contributing to the frontogenetic tendency of summer quasi-stationary fronts and that both terms tend to be too strong in the NAM forecast. The derivatives are computed with the 12-km grid spacing before interpolating to 0.25° for the FAD composite analyses.[2]

### d. Equitable threat score and bias

Equitable threat score (ETS; Schaefer 1990) and bias are commonly used metrics to evaluate precipitation forecasts that are utilized herein to evaluate precipitation forecasts within the frontal environments. These metrics are easily computed using a 2 × 2 contingency

[2] Because the data assimilation procedure used to generate the NAM analyses involves using an earlier NAM forecast as a background/first-guess field, the resolved scale of the forecasts and analyses is the same (G. DiMego, personal communication 2010). Thus, differences in the magnitude of terms involving spatial derivatives cannot simply be attributed to differences in resolved scale between forecasts and analyses. Sensitivity tests (not shown) using much coarser grids (~80-km grid spacing) to compute spatial derivatives verify that results are not sensitive to the grid spacing used to compute terms involving spatial derivatives.

table of possible forecast outcomes at individual grid points (e.g., Wilks 1995). The table elements consist of hits (correct forecast of an event), misses (observed but not forecast event), false alarms (forecast but not observed event), and correct negatives (correct forecast of nonevent). Using these elements, ETS is expressed as

$$\mathrm{ETS} = \frac{\mathrm{hits} - \mathrm{chance}}{\mathrm{hits} + \mathrm{misses} + \mathrm{false\ alarms} - \mathrm{chance}}, \quad (6)$$

where

$$\mathrm{chance} = \frac{(\mathrm{hits} + \mathrm{misses})(\mathrm{hits} + \mathrm{false\ alarms})}{\mathrm{hits} + \mathrm{misses} + \mathrm{correct\ negatives} + \mathrm{false\ alarms}}. \quad (7)$$

A perfect ETS is 1.0, the lower limit is $-1/3$, and scores below 0.0 indicate no skill. The ETS can be interpreted as the fraction of correctly predicted observed events, adjusted for hits associated with random chance. Bias is the ratio of forecast to observed events. Thus, the bias measures how well areal coverage of events is forecast. Bias greater (less) than 1.0 indicates overprediction (underprediction). In terms of contingency table elements, bias is expressed as

$$\mathrm{bias} = \frac{\mathrm{hits} + \mathrm{false\ alarms}}{\mathrm{hits} + \mathrm{misses}}. \quad (8)$$

## 3. Results

### *a. Composite structure*

Observed and simulated composite frontal environments constructed using the method outlined in section 2b are shown in Fig. 4 for the 900-hPa level. In the composite analysis (Fig. 4a), precipitation mainly occurs slightly north of the surface front and extends southeastward across the front, as indicated by a white dashed arrow following the ''core'' of precipitation contours. However, in the composite forecast, precipitation covers a much larger area along the front and is oriented nearly parallel to the front. Furthermore, the composite forecast precipitation has a close correspondence to the composite forecast DEF field, whereas in the analysis such a close correspondence does not exist (the correspondence will be verified statistically in section 3b). The pattern in 900-hPa winds near the main regions of precipitation in both analysis and forecast composites reflects the northern terminus of the LLJ and is characteristic of the warm-season pattern in which bow echoes travel along a quasi-stationary zonally oriented frontal boundary with a slight southeastward heading parallel to the midlevel northwesterly flow (Johns 1993; Coniglio et al. 2004; Wang et al. 2010).

While the NAM forecasts the general pattern in 900-hPa flow fairly well, the composite forecast of horizontal deformation (Fig. 4g) is too strong relative to the analysis (Fig. 4b). The overforecast deformation as well as the patterns in the forecast precipitation field is consistent with characteristics of the two cases illustrated in Figs. 1 and 2. On the other hand, differences between forecast and observed $|\nabla\theta|$ (Figs. 4g and 4b, respectively) are small relative to the differences in DEF, which is also a characteristic of the case in Fig. 2. Thus, it appears that if a thermodynamic field like $|\nabla\theta|$ is used to gauge frontal intensity, only small differences are discernable between composite observed and forecast fronts; however, if a kinematic field like DEF is used to gauge the frontal intensity, the composite forecast fronts are noticeably stronger than those observed. The same conclusion regarding frontal intensity based on thermodynamic versus kinematic fields is reached when examining low-level convergence rather than DEF, which is implied by the difference in composite forecast and observed $T_3$ fields (Figs. 4i and 4d, respectively) because $T_3$ is directly proportional to convergence. It is speculated that the more noticeable differences in the kinematic relative to the thermodynamic fields may simply reflect the fact that warm-season quasi-stationary fronts are often not well defined by temperature and/or moisture gradients (e.g., Johns 1984); rather, such fronts are more identifiable through wind shifts that are reflected in kinematic fields like horizontal deformation and convergence.

The overforecast DEF is reflected by the total frontogenesis $D|\nabla\theta|/Dt$, which has an amplitude that is nearly 2 times as large in the composite forecast (Fig. 4h) relative to the analysis (Fig. 4c). Examining the $T_3$ (Figs. 4c,h) and $T_4$ (Figs. 4d,i) terms of total frontogenesis separately shows that both terms contribute noticeably to the total frontogenesis differences between the composite forecast and analysis. Furthermore, in the analysis within the domain between $-2°$ and 4° in latitude along the front, the composite $T_4$ and $T_3$ together comprise 98% of the variance of $D|\nabla\theta|/Dt$, indicating the dominant role of $T_4$ and $T_3$ in the frontogenetic tendency. This feature is replicated in the NAM forecast (97%) and is consistent with previous studies analyzing slow-moving fronts (e.g., Hanstrum et al. 1990; Juang 1991).

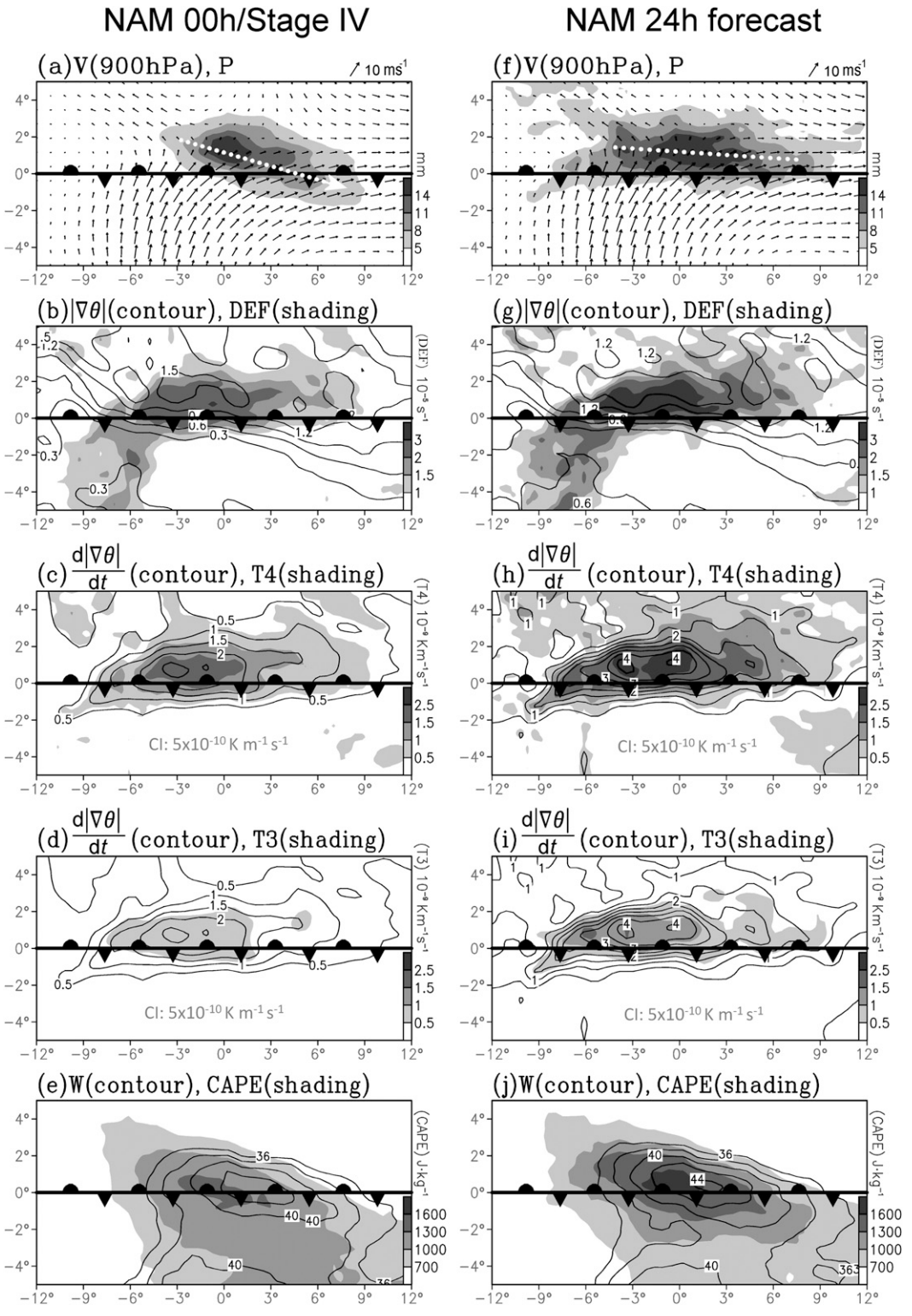


FIG. 4. Composite observed 900-hPa (a) wind vectors superimposed with 24-h accumulated stage-IV precipitation, (b) DEF (shadings) and $|\nabla\theta|$ (contours; interval is $3 \times 10^{-6}$ K m$^{-1}$), (c) $T_4$ (shadings) and (d) $T_3$ (shadings) superimposed with $d|\nabla\theta|/dt$ (contours; zero omitted), and (e) precipitable water (contours; interval is 2 g kg$^{-1}$) and CAPE (shadings). (f)–(j) As in (a)–(e), but for the 24-h NAM forecast. The precipitation orientation is indicated by white dashed lines in (a) and (f).

To inspect additional thermodynamics-related fields, composite forecast and observed surface-based CAPE and precipitable water are shown in Figs. 4j and 4e. The northwest–southeast-oriented patterns of CAPE and precipitable water are typical of the warm-season pattern (Coniglio et al. 2004; Tuttle and Davis 2006) and the spatial pattern in both fields is reasonably predicted by the NAM. However, CAPE and precipitable water are larger and more narrowly concentrated along the quasi-stationary front in the forecast than in the analysis, indicating that forecast frontal environments are too moist and unstable. Furthermore, the largest differences in CAPE between the composite forecast and analysis occur mainly north of the front and coincide with composite convective inhibition (CIN) that is about 20 J $kg^{-1}$ weaker in the forecast (not shown). Thus, the composite CAPE–CIN fields suggest easier convective initiation north of the front, which agrees with the precipitation bias.

Further insight into the composite frontal environments is revealed from the cross-front secondary circulation and the vertical sections of frontogenetic tendency across the FAD center (0° longitude with a ± 2° average; Fig. 5). The cross-front secondary circulation (i.e., mass-flux circulation) is depicted by model vertical velocity and meridional divergent winds computed from an iterative method introduced by Endlich (1967). Given the constraint of frontal angle relative to the latitude lines, it is assumed that the meridional mass-flux circulation across the FAD adequately represents the cross-frontal circulation, which normally should be perpendicular to the fronts. In the forecast (Fig. 5b), frontogenesis is tilted northward in the lower troposphere, consistent with the analysis (Fig. 5a), but is distinctly stronger than the analysis throughout the troposphere. The cross-front circulation is also noticeably stronger in the forecast, with an upright ascending branch immediately north of the surface front where the majority of precipitation occurs. The stronger ascending motion corresponds with the strong lower-level winds converging toward the front, which agrees with the stronger $T_3$ in the forecast (Fig. 4i). In addition, the stronger convergence of momentum enhances the convergence of water vapor flux toward the maximum precipitation area to the north of the surface front. These dynamical and moisture characteristics are likely associated with the excessive rainfall produced in the forecast.

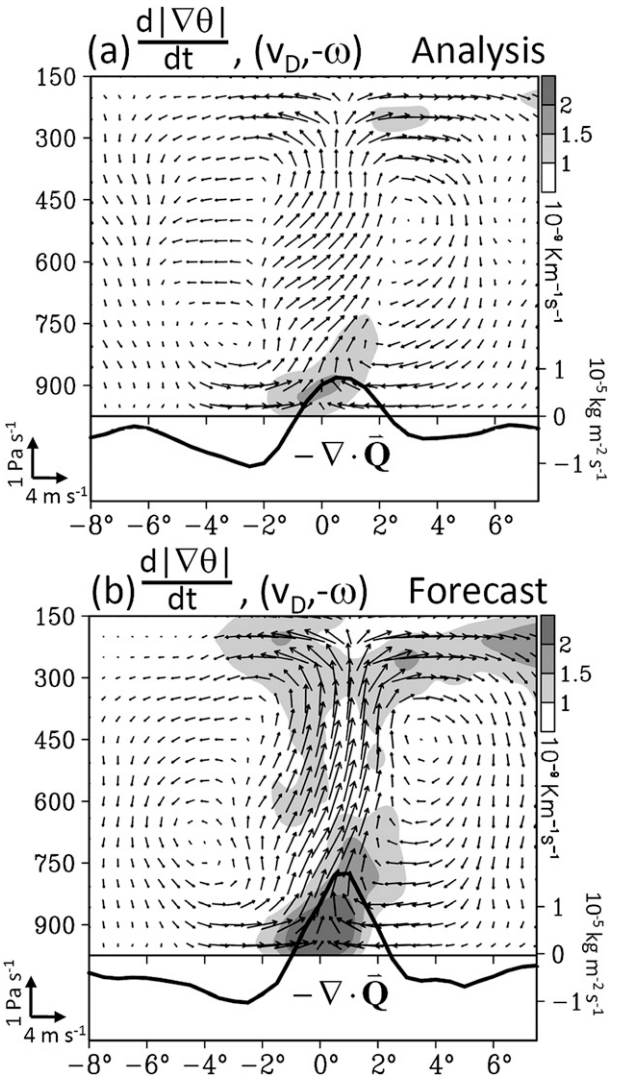


FIG. 5. Composite cross-frontal circulation (vectors) and vertical–meridional distributions of $d|\nabla\theta|/dt$ (shadings) superimposed with the convergence of water vapor flux (solid line) in the (a) analysis and (b) 24-h forecast.

### b. Statistics

To illustrate further the relationship between important frontogenesis terms and precipitation, a linear spatial correlation function is adopted. If we associate every grid cell $i$ in the FAD with a random variable $F_i$ and denote its variance as $\sigma^2_{F_i}$, then for the parameters of interest at two different grid cells $i$ and $j$ the spatial correlation between the parameters at grid cell $i$ and $j$ is given by

$$\rho_{i,j} \equiv \mathrm{cov}(F_i, F_j)/(\sigma_{F_i}\sigma_{F_j}), \tag{9}$$

where $\mathrm{cov}(F_i, F_j)$ is the covariance between $F_i$ and $F_j$. The spatial correlation within the FAD is computed between precipitation and 900-hPa deformation in each individual case, which is then averaged for all cases, as is shown in Fig. 6a. The error bar at each forecast hour depicts 1 standard deviation while the confidence level (CL) is estimated from the $t$ statistic. In the analysis, the correlation between the precipitation pattern and the deformation pattern is at the 95% CL but below the

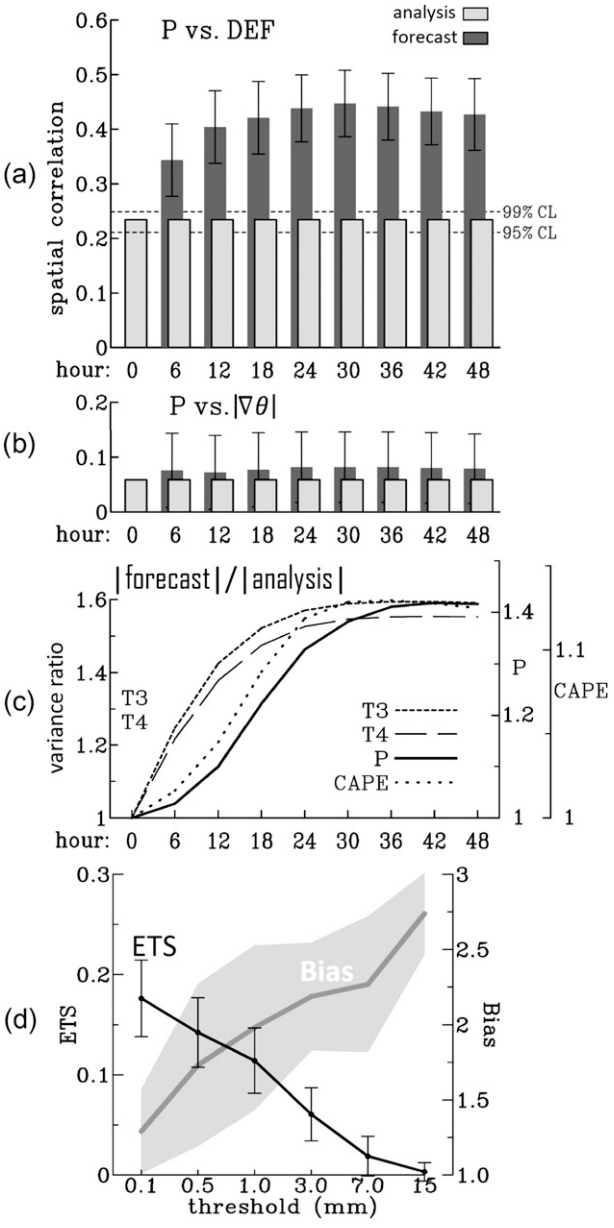


FIG. 6. (a) Spatial correlation coefficients between precipitation and the 900-hPa deformation for hours 0–48 in the forecast (dark bars) and the analysis (light bars). The analysis is repeated throughout the forecast cycle for easy comparison. (b) As in (a), but between precipitation and $\nabla\theta$. Statistical CLs are indicated in (a). (c) Variance ratios of $T_3$, $T_4$, precipitation, and CAPE within the FAD, with legend in the lower right. Each variable is adjusted to have its maximum ratio at later hours aligned together, and each has a corresponding $y$ axis. (d) Mean ETSs (solid line with error bars) and biases (gray line with error shadings) of the 24-h forecast at various thresholds.

99% CL. In the forecast, however, the correlation is well above the 99% CL and, after hour 18, becomes 2 times as large as in the analysis. For precipitation and $|\nabla\theta|$ (Fig. 6b), the spatial correlation in the analysis is insignificant, although the forecast reveals a slightly stronger correlation (but still insignificant). Thus, there is a spurious coherence between precipitation and deformation in the NAM forecasts, as was observed in the case examples (Figs. 1 and 2).

An attempt is made to understand whether the bias in kinematic fields leads to the bias in precipitation, or vice versa. By comparing the variance of each variable in the forecast with that in the analysis, one obtains a variance ratio reflecting the intensity error of the forecast within the FAD. We use variance instead of area-average magnitude not only to reveal the error but to highlight the contrast of biases between the frontal zone and its surroundings, as is shown in Fig. 4. Calculating the variance ratio throughout the forecast hours indicates the error growth. As shown in Fig. 6c, the error growth of $T_3$ and $T_4$ clearly leads the error growth of precipitation and CAPE. This result seems to imply that biases in precipitation/CAPE may be induced from biases in the kinematic fields. However, there are other possible explanations for the lag in errors between these fields (discussed later in section 4), so that further work is needed to firmly establish a physical linkage between them.

The impact of these errors on frontal rainfall forecasts is substantiated through ETSs and bias computed with the 12-km grid spacing within the FAD. As shown in Fig. 6d, ETSs in the 24-h forecast are generally low and the scores decline substantially with increasing rainfall thresholds. In the meantime, bias increases with increasing rainfall thresholds. The ETS and bias results are indicative of forecast rainfall that is too widespread and displaced relative to observations, which is generally consistent with the observed and forecast rainfall composites (Figs. 4a and 4f). Similar precipitation biases were also noted by Wang et al. (2009) in which similar types of cases related to midtropospheric perturbations were examined. Wang et al. attributed the widespread and displaced forecast rainfall to the overall slower propagation of midtropospheric perturbations that often accompany progressive MCSs. Nevertheless, these statistical results provide additional and quantitative evidence to complement the composite analysis.

## 4. Summary and discussion

Zonally oriented, quasi-stationary surface fronts are common synoptic features in the warm season pattern crucial to central U.S. summer rainfall. Using a composite procedure, this study examined NAM forecast and observed environments associated with such fronts for 64 cases that occurred during the period July–August 2006–08. It was found that the NAM did well at depicting the general synoptic features associated with the

frontal environments such as the patterns in low-level wind and CAPE fields, as well as the positions of the fronts. However, kinematic fields important to frontogenesis such as deformation and horizontal convergence were overpredicted in the NAM. Perhaps related to the overprediction of these kinematic fields through convergence of water vapor flux, CAPE andprecipitable water were also overpredicted, and the cross-frontal secondary circulation was too strong. In addition, through analysis of spatial correlation coefficients for the individual cases, it was found that the relationship between deformation and precipitation was much more robust in the forecasts than in the analyses, indicating a spurious coherence between these two fields in the NAM. This spurious coherence was also consistent with the close correspondence between forecast precipitation and deformation observed in frontal composites.

There were very distinct differences in the spatial distribution of precipitation within the frontal environments between the NAM forecasts and corresponding analyses. The forecasts featured a broad area of precipitation that stretched along a relatively large region parallel to the front, while the area of precipitation in the analyses covered a smaller area and was oriented from WNW to ESE relative to the front, with the southernmost portion of precipitation stretching across the front. The orientation of the observed precipitation is consistent with typical paths of derecho-producing MCSs examined by Johns and Hirt (1987) that initiate north of a quasi-stationary low-level boundary and move parallel to the boundary at a slight angle toward the warm sector, following the midtropospheric northwesterly flow. Thus, because the warm-season quasi-stationary boundaries examined herein are typically associated with MCSs, it seems likely that the deficiencies in NAM at least partially result from the inability to depict MCSs properly, which is not surprising since numerous previous works (e.g., Weisman et al. 1997; Davis et al. 2003; Clark et al. 2007) have documented problems in simulating propagating MCSs using grid spacing that requires CP. However, it also seems likely that problems with the NAM model precipitation forecasts could be related to the overprediction of the kinematic fields related to frontogenesis, like deformation and convergence, as is suggested in Fig. 6c.

From our analysis it is not possible to diagnose what caused the overprediction in these kinematic fields, but we speculate that it is related to the physics parameterizations used in the NAM. For example, the shallow component of the BMJ CP tends to erode capping inversions in frontal environments, similar to observations made by Baldwin et al. (2002). Widespread activation of the deep convection component of the BMJ scheme within frontal environments could then induce enhanced low-level convergence into regions where parameterized convection occurs. This scenario would seem to imply that the biases in precipitation and kinematic fields would appear at the same time, in contrast with Fig. 6c, which shows biases in precipitation lagging biases in frontogenesis terms. However, it is possible that kinematic fields simply respond more quickly to the activation of deep convection, whereas precipitation must accumulate for a while before positive biases become apparent. It is also entirely possible that there is some other dynamical mechanism responsible for the overpredicted kinematic fields that are coherent with the overpredicted and displaced rainfall. In any case, further investigation is needed to diagnose the NAM deficiencies related to frontal environments that have been documented. Regardless of the cause of the deficiencies, recognition of the environments associated with such errors should be valuable to operational forecasters. In addition, it would be useful to use a similar procedure to evaluate the forecasts of frontal environments in convection-allowing simulations.

*Acknowledgments.* Valuable comments offered by William Gallus and two anonymous reviewers are highly appreciated. SYW is supported by the USDA–CSREES-funded Drought Management, Utah Project, and AJC is supported through a National Research Council postdoctoral award.

## REFERENCES

Accadia, C., S. Mariani, M. Casaioli, A. Lavagnini, and A. Speranza, 2003: Sensitivity of precipitation forecast skill scores to bilinear and a simple nearest-neighbor average method on high-resolution verification grids. *Wea. Forecasting,* **18,** 918–932.

Baldwin, M. E., J. S. Kain, and M. P. Kay, 2002: Properties of the convection scheme in NCEP's Eta Model that affect forecast sounding interpretation. *Wea. Forecasting,* **17,** 1063–1079.

Betts, A. K., 1986: A new convective adjustment scheme. Part I: Observational and theoretical basis. *Quart. J. Roy. Meteor. Soc.,* **112,** 677–691.

——, and M. J. Miller, 1986: A new convective adjustment scheme. Part II: Single-column tests using GATE wave, BOMEX, ATEX and Arctic air-mass data sets. *Quart. J. Roy. Meteor. Soc.,* **112,** 693–709.

Bukovsky, M. S., J. S. Kain, and M. E. Baldwin, 2006: Bowing convective systems in a popular operational model: Are they for real? *Wea. Forecasting,* **21,** 307–324.

Clark, A. J., W. A. Gallus Jr., and T.-C. Chen, 2007: Comparison of the diurnal precipitation cycle in convective-resolving and non-convection-resolving mesoscale models. *Mon. Wea. Rev.,* **135,** 3456–3473.

——, ——, M. Xue, and F. Kong, 2009: A comparison of precipitation forecast skill between small convection-allowing and

large convection-parameterizing ensembles. *Wea. Forecasting,* **24,** 1121–1140.

Coniglio, M. C., and D. J. Stensrud, 2001: Simulation of a progressive derecho using composite initial conditions. *Mon. Wea. Rev.,* **129,** 1593–1616.

——, ——, and M. B. Richman, 2004: An observational study of derecho-producing convective systems. *Wea. Forecasting,* **19,** 320–337.

——, K. L. Elmore, J. S. Kain, S. J. Weiss, M. Xue, and M. Weisman, 2009: Evaluation of WRF model output for severe weather forecasting from the 2008 NOAA Hazardous Weather Testbed Spring Experiment. *Wea. Forecasting,* **25,** 408–427.

Davis, C. A., K. W. Manning, R. E. Carbone, S. B. Trier, and J. D. Tuttle, 2003: Coherence of warm-season continental rainfall in numerical weather prediction models. *Mon. Wea. Rev.,* **131,** 2667–2679.

Du, J., and Coauthors, 2004: The NOAA/NWS/NCEP Short Range Ensemble Forecast (SREF) system: Evaluation of an initial condition vs multiple model physics ensemble approach. Preprints, *20th Conf. on Weather Analysis and Forecasting/16th Conf. on Numerical Weather Prediction,* Seattle, WA, Amer. Meteor. Soc., 21.3. [Available online at http://ams.confex.com/ams/pdfpapers/71107.pdf.]

Endlich, R. M., 1967: An iterative method for altering the kinematic properties of wind fields. *J. Appl. Meteor.,* **6,** 837–844.

Ferrier, B. S., Y. Jin, Y. Lin, T. Black, E. Rogers, and G. DiMego, 2002: Implementation of a new grid-scale cloud and rainfall scheme in the NCEP Eta Model. Preprints, *15th Conf. on Numerical Weather Prediction,* San Antonio, TX, Amer. Meteor. Soc., 280–283.

Fritsch, J. M., and R. E. Carbone, 2004: Improving quantitative precipitation forecasts in the warm season: A USWRP research and development strategy. *Bull. Amer. Meteor. Soc.,* **85,** 955–965.

——, R. Kane, and C. Chelius, 1986: The contribution of mesoscale convective weather systems to the warm-season precipitation in the United States. *J. Appl. Meteor.,* **25,** 1333–1345.

Hanstrum, B., K. Wilson, and S. Barrell, 1990: Prefrontal troughs over southern Australia. Part II: A case study of frontogenesis. *Wea. Forecasting,* **5,** 32–46.

Higgins, R. W., Y. Yao, E. S. Yarosh, J. E. Janowiak, and K. C. Mo, 1997: Influence of the Great Plains low-level jet on summertime precipitation and moisture transport over the central United States. *J. Climate,* **10,** 481–507.

Hohenegger, C., and C. Schar, 2007: Atmospheric predictability at synoptic versus cloud-resolving scales. *Bull. Amer. Meteor. Soc.,* **88,** 1783–1793.

Janjić, Z. I., 1994: The step-mountain eta coordinate model: Further developments of the convection, viscous sublayer, and turbulence closure schemes. *Mon. Wea. Rev.,* **122,** 927–945.

——, 2002: Nonsingular implementation of the Mellor–Yamada level 2.5 scheme in the NCEP Meso-model. NCEP Office Note 437, 61 pp.

——, 2003: A nonhydrostatic model based on a new approach. *Meteor. Atmos. Phys.,* **82,** 271–285.

Johns, R. H., 1984: A synoptic climatology of northwest flow severe weather outbreaks. Part II: Meteorological parameters and synoptic patterns. *Mon. Wea. Rev.,* **112,** 449–464.

——, 1993: Meteorological conditions associated with bow echo development in convective storms. *Wea. Forecasting,* **8,** 294–299.

——, and W. D. Hirt, 1987: Derechos: Widespread convectively induced windstorms. *Wea. Forecasting,* **2,** 32–49.

Juang, H. M.-H., 1991: Numerical simulations of the evolution of a cold front and its precipitation. *Mon. Wea. Rev.,* **119,** 385–411.

Knievel, J. C., and R. H. Johnson, 2002: The kinematics of a midlatitude, continental mesoscale convective system and its mesoscale vortex. *Mon. Wea. Rev.,* **130,** 1749–1770.

Kong, F., K. K. Droegemeier, and N. L. Hickmon, 2006: Multiresolution ensemble forecasts of an observed tornadic thunderstorm system. Part I: Comparison of coarse and fine-grid experiments. *Mon. Wea. Rev.,* **134,** 807–833.

Lin, Y., and K. E. Mitchell, 2005: The NCEP stage II/IV hourly precipitation analyses: Development and applications. Preprints, *19th Conf. on Hydrology,* San Diego, CA, Amer. Meteor. Soc., 1.2. [Available online at http://ams.confex.com/ams/pdfpapers/83847.pdf.]

Liu, C., M. W. Moncrieff, J. D. Tuttle, and R. E. Carbone, 2006: Explicit and parameterized episodes of warm-season precipitation over the continental United States. *Adv. Atmos. Sci.,* **23,** 91–105.

Martin, J. E., Ed., 2006: The vertical circulation at fronts. *Mid-Latitude Atmospheric Dynamics: A First Course,* John Wiley and Sons, 187–234.

Mellor, G. L., and T. Yamada, 1982: Development of a turbulence closure model for geophysical fluid problems. *Rev. Geophys.,* **20,** 851–875.

Molinari, J., and M. Dudek, 1992: Parameterization of convective precipitation in mesoscale numerical models: A critical review. *Mon. Wea. Rev.,* **120,** 326–344.

Schaefer, J. T., 1990: The critical success index as an indicator of warning skill. *Wea. Forecasting,* **5,** 570–575.

Schmidt, J. M., and W. R. Cotton, 1989: A high plains squall line associated with severe surface winds. *J. Atmos. Sci.,* **46,** 281–302.

Segal, M., J. Garratt, G. Kallos, and R. Pielke, 1989: The impact of wet soil and canopy temperatures on daytime boundary-layer growth. *J. Atmos. Sci.,* **46,** 3673–3684.

Smull, B. F., and J. A. Augustine, 1993: Multiscale analysis of a mature mesoscale convective complex. *Mon. Wea. Rev.,* **121,** 103–132.

Tuttle, J. D., and C. A. Davis, 2006: Corridors of warm season precipitation in the central United States. *Mon. Wea. Rev.,* **134,** 2297–2317.

Walser, A., D. Lüthi, and C. Schär, 2004: Predictability of precipitation in a cloud-resolving model. *Mon. Wea. Rev.,* **132,** 560–577.

Wang, S.-Y., and T.-C. Chen, 2009: The late spring maximum of rainfall over the United States central plains and the role of the low-level jet. *J. Climate,* **22,** 4696–4709.

——, ——, and S. E. Taylor, 2009: Evaluations of NAM forecasts on midtropospheric perturbation-induced convective storms over the U.S. northern plains. *Wea. Forecasting,* **24,** 1309–1333.

——, ——, and J. Correia Jr., 2010: Climatology of summer midtropospheric perturbations in the U.S. northern plains. Part I: Influence on northwest flow severe weather outbreaks. *Climate Dyn.,* doi:10.1007/s00382-009-0696-3, in press.

Weisman, M. L., W. C. Skamarock, and J. B. Klemp, 1997: The resolution dependence of explicitly modeled convective systems. *Mon. Wea. Rev.,* **125,** 527–548.

Weisman, R. A., 1990: An observational study of warm season southern Appalachian lee troughs. Part II: Thunderstorm genesis zones. *Mon. Wea. Rev.,* **118,** 2020–2041.

Wilks, D. S., 1995: *Statistical Methods in the Atmospheric Sciences: An Introduction*. Academic Press, 467 pp.